

# Dual Directional Expansion of Classical Cepheids in the Small Magellanic Cloud Revealed by *Gaia* DR3

SATOYA NAKANO (中野 寛矢) <sup>1</sup> AND KENGO TACHIHARA (立原 研悟) <sup>1</sup>

<sup>1</sup>*Nagoya University, Nagoya, Aichi, 464-8602 Japan*

## ABSTRACT

We present the three-dimensional kinematics of classical Cepheids (CCs) in the Small Magellanic Cloud (SMC) using *Gaia* DR3 data. By cross-matching the CCs obtained from the fourth phase of the Optical Gravitational Lensing Experiment with *Gaia* DR3, we obtain distances and proper motions (PMs) for 4,236 CCs. Among them, 91 stars with available radial velocities (RVs) enable the construction of accurate relationship between distance and RV. Furthermore, we calculate the internal PMs of the CCs, providing the internal dynamics of the SMC while removing the distance projection effects. The CCs exhibit a northeast-southwest distance gradient, with internal PMs pointing northeast for nearer stars and southwest for more distant stars, indicating a northeast-southwest elongation. The RVs of the CCs show a northwest-southeast gradient, consistent with RVs of other stellar populations and suggesting that the SMC's northwest-southeast elongation results from interactions with the Large Magellanic Cloud. The distances and RVs of the CCs are nearly uncorrelated, implying that the two elongations arise from distinct causes.

**Keywords:** Cepheid distance (217) — Small Magellanic Cloud (1468) — Galaxy interaction (600) — Proper motions (1295) — Radial velocity (1332) — *Gaia* (2360)

## 1. INTRODUCTION

The Small Magellanic Cloud (SMC), located at  $\sim 60$  kpc (R. de Grijs & G. Bono 2015), together with the Large Magellanic Cloud (LMC) at  $\sim 50$  kpc (R. de Grijs et al. 2014), represents the nearest interacting galaxy system to the Milky Way.

Understanding the internal kinematics of the two Magellanic galaxies is crucial for reconstructing their interaction history with the Milky Way and their evolutionary pathways. The kinematic signatures of the SMC and LMC are likely imprinted in the motions of the Magellanic Stream (D. S. Mathewson et al. 1974) and Bridge (J. V. Hindman et al. 1963; M. J. Irwin et al. 1985), thought to have formed from material stripped from these galaxies. Accurately reproducing these features is essential for constraining their orbital histories (e.g., G. Besla et al. 2007, 2012; J. D. Diaz & K. Bekki 2012; M. Salem et al. 2015). Additionally, the rotation curves of the galaxies provide key constraints on their

masses, a fundamental parameter in gravitational interactions.

The mass of the SMC has traditionally been estimated using its rotation curve derived from H I emission line observations (S. Stanimirović et al. 2004; E. M. Di Teodoro et al. 2019). However, recent studies based on proper motions (PMs) and radial velocities (RVs) of various stellar populations have highlighted discrepancies between the three-dimensional stellar kinematics and the H I rotation (C. E. Murray et al. 2019; M. De Leo et al. 2020; F. Niederhofer et al. 2021; S. Nakano et al. 2025). These findings suggest that the velocity gradient observed in H I may not reflect true galactic rotation but rather result from tidal interactions.

Interpreting the kinematics of the SMC is complicated by its significant line-of-sight depth. For example, classical Cepheids (CCs; V. Ripepi et al. 2017) and RR Lyrae stars (A. M. Jacyszyn-Dobrzaniecka et al. 2017) suggest tidal stretching, with a line-of-sight extent of  $\sim 20$ – $30$  kpc. Thus, the precise locations of H I and the young stars tracing it within the 50 to 80 kpc range remain unclear. The multiple line-of-sight velocity components of H I observed in the SMC may result from overlapping structures at different distances (e.g., E. Muller & K. Bekki 2007). Furthermore, since the apparent PM of

Corresponding author: Satoya Nakano  
nasatoya@a.phys.nagoya-u.ac.jp

objects depends on their distance, accurate determining the direction and magnitude of internal PMs requires precise stellar distance measurements.

Discussing the internal PMs of CCs, which have accurately determined distances, is important for understanding the dynamics of the SMC. [F. Niederhofer et al. \(2021\)](#) emphasized the impact of distance on estimating internal PMs and cross-matched the CCs from [V. Ripepi et al. \(2017\)](#) with *Gaia* Data Release 2 (DR2) to examine their motion, accounting for distance. Their results showed that nearer CCs are moving northeast relative to more distant ones, suggesting that stars in the vicinity are being stripped from the SMC. However, due to the limited RV data for the CCs in *Gaia* DR2, [F. Niederhofer et al. \(2021\)](#) had to rely on RVs from younger stellar populations ([C. J. Evans & I. D. Howarth 2008](#)) for their analysis. Since the spatial distribution of CCs lacks the clear Wing structure seen in young stars or the interstellar medium (ISM), it remains uncertain whether the RVs of CCs align with those of young stars.

The relationship between the distances and RVs of stars in the SMC is also crucial for comparisons with theoretical simulations. [J. D. Diaz & K. Bekki \(2012\)](#) modeled the SMC as a spheroid and a rotating disk, simulating its interactions with the LMC and the Milky Way. Their results showed that the disk reproduced a northeast-southwest line-of-sight velocity gradient, consistent with H I observations, while the spheroid produced a northwest-southeast gradient. Both components displayed line-of-sight velocity amplitudes of  $\sim 100\text{--}200 \text{ km s}^{-1}$ . The spheroid's velocity gradient was interpreted as a result of tidal forces from the LMC, located to the southeast, and it differed in angle from the H I velocity gradient. Furthermore, they demonstrated that the disk component forms a tidal arm, the Counter-Bridge, alongside the Magellanic Bridge. The Counter-Bridge extends behind the SMC in an arc toward the LMC, with an observational signature of increasing RVs with distance, spanning  $\sim 100\text{--}200 \text{ km s}^{-1}$ —similar to the SMC's main body. [J. D. Diaz & K. Bekki \(2012\)](#) emphasized that correlating distances with RVs is key to validating the Counter-Bridge, as it overlaps with the SMC's line-of-sight.

In this study, we present the first internal PM map of the SMC that accounts for its large line-of-sight depth by cross-matching the CCs from [V. Ripepi et al. \(2017\)](#) with *Gaia* DR3 ([Gaia Collaboration et al. 2016, 2023](#)). As *Gaia* DR3 provides RV measurements for sufficiently bright ( $G \lesssim 15 \text{ mag}$ ) stars, a key feature of this work is the accurate relationship between distances and RVs for the SMC's bright CCs. Our *Gaia* DR3 sample includes 91 CCs with available RVs, a significant increase from

the 8 CCs from *Gaia* DR2. Furthermore, we identify young massive Cepheids as gas tracers by selecting massive star candidates ( $M_{\text{ini}} \geq 8M_{\odot}$ ,  $\text{Age} \lesssim 50.0 \text{ Myr}$ ) from [S. Nakano et al. \(2025\)](#), using the *Gaia* color-magnitude diagram. [J. D. Diaz & K. Bekki \(2012\)](#) suggests that the Counter-Bridge may only be observable in young stellar populations, similar to the Magellanic Bridge. Therefore, identifying particularly young stars among the CCs is crucial. We describe the sample and internal PM calculation method in Section 2, present the results in Section 3, and discuss the relationship between the distances and RVs of CCs and their spatial distribution compared to the velocity components of H I in Section 4.

For this paper, we adopt a representative distance to the SMC of  $D_{\text{SMC}} = 62 \text{ kpc}$  ([D. Graczyk et al. 2014](#); [R. de Grijs & G. Bono 2015](#)).

## 2. SAMPLE OF CLASSICAL CEPHEIDS

### 2.1. Distance Calculation for CCs

For the catalog of Cepheids in the SMC, we downloaded the data of CCs associated with the SMC from the database of the fourth phase of the Optical Gravitational Lensing Experiment<sup>1</sup> (OGLE-IV survey; [A. Udalski et al. 2015](#); [I. Soszyński et al. 2015](#)). We use the celestial coordinates and  $V$  magnitudes from the OGLE-IV data. The CCs are then matched with the pulsation modes and periods ( $P$ ) of OGLE CCs listed in Table 2 of [V. Ripepi et al. \(2017\)](#), along with the  $K$ s magnitudes from the VISTA near-infrared YJKs survey of the Magellanic System (VMC survey; [M. R. L. Cioni et al. 2011](#)). In total, 4793 CCs are successfully matched.

To determine the distances of these CCs, we adopt the method suggested by [V. Ripepi et al. \(2016, 2017\)](#). They established a reddening-free distance estimation method by deriving a more precise period–Wesenheit ( $PW$ ) relation using near-infrared observational data, rather than the conventional period–luminosity ( $PL$ ) relation. We adopt the following  $PW$  relation, using the Wesenheit index  $W(V, Ks) = Ks - 0.13(V - Ks)$ :

$$W(V, Ks) = \alpha \log P + \beta, \quad (1)$$

where  $\alpha$  and  $\beta$  are constants that depend on the pulsation modes, as determined by [V. Ripepi et al. \(2017\)](#). The specific values of  $\alpha$  and  $\beta$  are listed in Table 3 of [V. Ripepi et al. \(2017\)](#). Since values of  $\alpha$  and  $\beta$  for mixed modes are not provided, we exclude 290 mixed-mode CCs from our sample.

<sup>1</sup> The OGLE Cepheids catalog can be downloaded from <https://ogledb.astrouw.edu.pl/~ogle/OCVS/ceph-query.php>.

The distance of the CCs,  $D_{\text{star}}$ , is calculated using the following equation:

$$D_{\text{star}}(V, Ks) = D_{\text{SMC}} 10^{\Delta W(V, Ks)}, \quad (2)$$

where  $\Delta W(V, Ks) = W(V, Ks) - (\alpha \log P + \beta)$ . For each pulsation mode, we iteratively apply a  $3.5\sigma$ -clipping procedure to  $\Delta W(V, Ks)$  until convergence, excluding 257 CCs from the sample in the process. V. Ripepi et al. (2017) adopted a distance to the SMC of 63 kpc, whereas we use  $D_{\text{SMC}} = 62$  kpc (R. de Grijs & G. Bono 2015), consistent with the 62.1 kpc (D. Graczyk et al. 2014) used by F. Niederhofer et al. (2021).

Through the above calculations, we obtain  $D_{\text{star}}$  for a total of 4,246 CCs. The mean  $D_{\text{star}}$  of the CCs we calculated is 62.2 kpc. The range of  $D_{\text{star}}$  for the CCs extends from  $\sim 50$ –80 kpc, which is consistent with the results of V. Ripepi et al. (2017).

## 2.2. Cross-matching with *Gaia* DR3

We cross-match the 4,246 CCs obtained in Section 2.1 with *Gaia* DR3. A cross-match radius of 0.5 arcsec is adopted, and *Gaia* DR3 counterparts are found for all CCs. However, eight CCs have two *Gaia* DR3 sources within the radius. To ensure reliability, we exclude them from our sample<sup>2</sup>. By further removing sources without available PM measurements, our final CC sample consists of 4,236 objects. Hereafter, we refer to these 4,236 CCs simply as the CC samples. A complete list of the CC samples, along with various physical parameters, is provided in Appendix A.

Below, the PM in the RA direction, corrected for coordinate distortion by multiplying with  $\cos \delta$ , is denoted as  $\mu_\alpha$ , while the PM in the DEC direction is denoted as  $\mu_\delta$ . For the CC samples, the mean errors of  $\mu_\alpha$  and  $\mu_\delta$  are (0.075, 0.069) mas yr<sup>-1</sup>. The tangential velocities in units of km s<sup>-1</sup> are obtained by multiplying the PMs by  $4.7438 \times D_{\text{star}}$  (kpc). For the CC samples, the mean errors of the tangential velocities are (23.3, 23.0) km s<sup>-1</sup>, assuming a uniform uncertainty of 1.6 kpc for  $D_{\text{star}}$ , following V. Ripepi et al. (2017).

Among the CC samples, RVs are available for 91 bright stars with  $G \lesssim 15$  mag. The mean RV is 150.25 km s<sup>-1</sup>, and the mean error of RV is 5.46 km s<sup>-1</sup>. Here, RVs are referenced to the solar system barycentric frame.

Figure 1 shows  $(G_{\text{BP}} - G_{\text{RP}}, G)$  color-magnitude diagram (CMD) of the CC samples<sup>3</sup>, along with the mas-

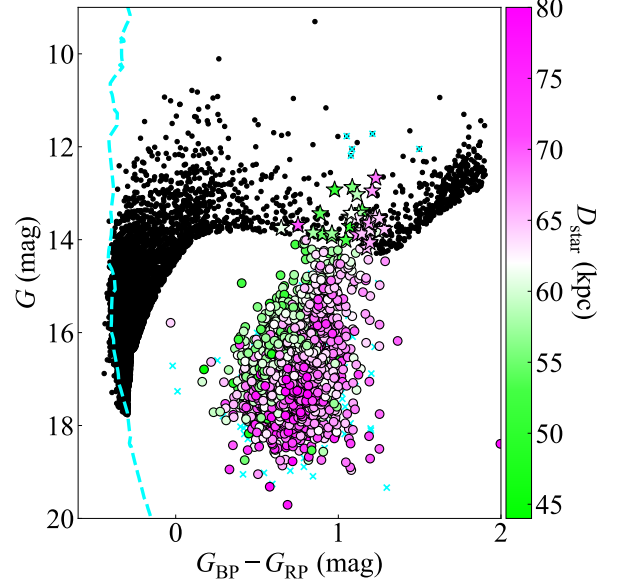


**Figure 1.** The  $(G_{\text{BP}} - G_{\text{RP}}, G)$  CMD of the CC samples. The colored circles and star symbols represent the CC samples, with their colors indicating the respective values of  $D_{\text{star}}$ . The black circles represent massive star candidates ( $M_{\text{ini}} \geq 8M_\odot$ , Age  $\lesssim 50.0$  Myr; S. Nakano et al. 2025). The colored star symbols represent massive Cepheids, corresponding to 38 massive star candidates among the CC samples. The cyan crosses represent 543 objects that have counterparts in *Gaia* DR3 but were excluded from the CC samples due to either the  $3.5\sigma$ -clipping applied to  $\Delta W(V, Ks)$  or the lack of available PM data. The cyan dashed line represents an approximate main sequence constructed using isochrones of the PARSEC (version 1.2S; A. Bressan et al. 2012; Y. Chen et al. 2014, 2015; J. Tang et al. 2014; P. Marigo et al. 2017; G. Pastorelli et al. 2019, 2020). The metallicity of the main sequence is assumed to be  $Z = 0.1Z_\odot$ , with  $Z_\odot = 0.0152$ . Additionally, a reddening correction of  $A_V = 0.15$  mag due to the Milky Way foreground is applied to the main sequence using *dustapprox* (M. Fousneau et al. 2022).

sive star candidates identified by S. Nakano et al. (2025). The CC samples are concentrated in a specific region of the CMD corresponding to the Cepheid instability strip, supporting the accuracy of the cross-matching. More distant CCs tend to be distributed toward the redder side of the CMD, likely reflects the increasing amount of intervening foreground dust along the line-of-sight.

<sup>2</sup> The OGLE-IDs of the excluded objects are OGLE-SMC-CEP-1060, 1617, 1623, 2683, 2752, 2863, 3593, and 4101.

<sup>3</sup> Six CCs lack available  $G_{\text{BP}} - G_{\text{RP}}$  values and are therefore not plotted in Figure 1.

Additionally, 38 CCs overlap with the massive star candidates<sup>4</sup>. These massive Cepheids can be regarded as gas tracers, satisfying  $M_{\text{ini}} \geq 8M_{\odot}$  and  $\text{Age} \lesssim 50.0$  Myr (S. Nakano et al. 2025). Among them, RVs are available for 37 objects. The mean RV calculated from only the massive Cepheids is  $153.63 \text{ km s}^{-1}$ , with a mean RV error of  $3.75 \text{ km s}^{-1}$ .

### 2.3. Calculation of Internal PMs

For the calculation of internal PMs, we adopt a method similar to that of S. Nakano et al. (2025). Specifically, we compute the internal PMs by subtracting the systemic PM of the SMC from the PMs of the CC samples. However, S. Nakano et al. (2025) suggested that the spatial distribution and kinematics of massive star candidates with  $\text{Age} \lesssim 50.0$  Myr differ from those of older populations. It is not necessarily evident whether CCs with  $\text{Age} \sim 200$  Myr (V. Ripepi et al. 2017) follow the same kinematics as older populations. Therefore, we adopt the mean PM of the CC samples as the systemic PM of the SMC for the calculation of their internal PMs. The internal PMs calculated using the mean PM of the massive star candidates from S. Nakano et al. (2025) as the systemic PM are presented in Appendix B.

To compute the mean PM, we select 4,105 objects from the CC samples that fall within  $\pm 2\sigma$  in both  $\mu_{\alpha}$  and  $\mu_{\delta}$ . Hereafter, we refer to these 4,105 objects, to which the  $2\sigma$ -cutoff is applied, as the clipped CC samples. To account for coordinate distortions, we transform the coordinates to an orthographic projection following Gaia Collaboration et al. (2018). For this transformation, we adopt the coordinate center as the center of the CC distribution,  $(\alpha_{\text{cep}}, \delta_{\text{cep}}) = (12.54^{\circ}, -73.11^{\circ})$ , derived by V. Ripepi et al. (2017). Under the orthographic projection, the mean PM of the clipped CC samples is  $(\mu_{\alpha}, \mu_{\delta}) = (0.705, -1.265) \text{ mas yr}^{-1}$ .

This value is close to that derived by F. Niederhofer et al. (2021), which was obtained by assuming the center of the CC distribution based on data including older populations from the VMC survey,  $(0.734 \pm 0.008, -1.234 \pm 0.008) \text{ mas yr}^{-1}$ , but it does not agree within the error range. Since the overall characteristics of the internal PMs remain unchanged regardless of which value is used, we adopt the mean PM of the clipped CC samples as the systemic PM for the internal PMs calculation.

Since the  $D_{\text{star}}$  for CCs are well determined, we subtract the mean PM using equation (6) of S. Nakano et al. (2025). After subtracting the mean PM, we perform an inverse transformation from the orthographic projection to restore the coordinates to the equatorial frame. Through this procedure, we obtain the internal PMs of the CC samples, which are provided in Section A.

Note that, the magnitude of the mean PM corresponds to a tangential velocity of  $\sim 400 \text{ km s}^{-1}$ . Stars with extreme distances near 50 kpc or 80 kpc deviate by approximately 25% from  $D_{\text{SMC}}$ , meaning that neglecting  $D_{\text{star}}$  in the internal PMs calculation can introduce errors of up to  $\sim 100 \text{ km s}^{-1}$ . This highlights the importance of accounting for  $D_{\text{star}}$  when computing the internal PMs of the CC samples.

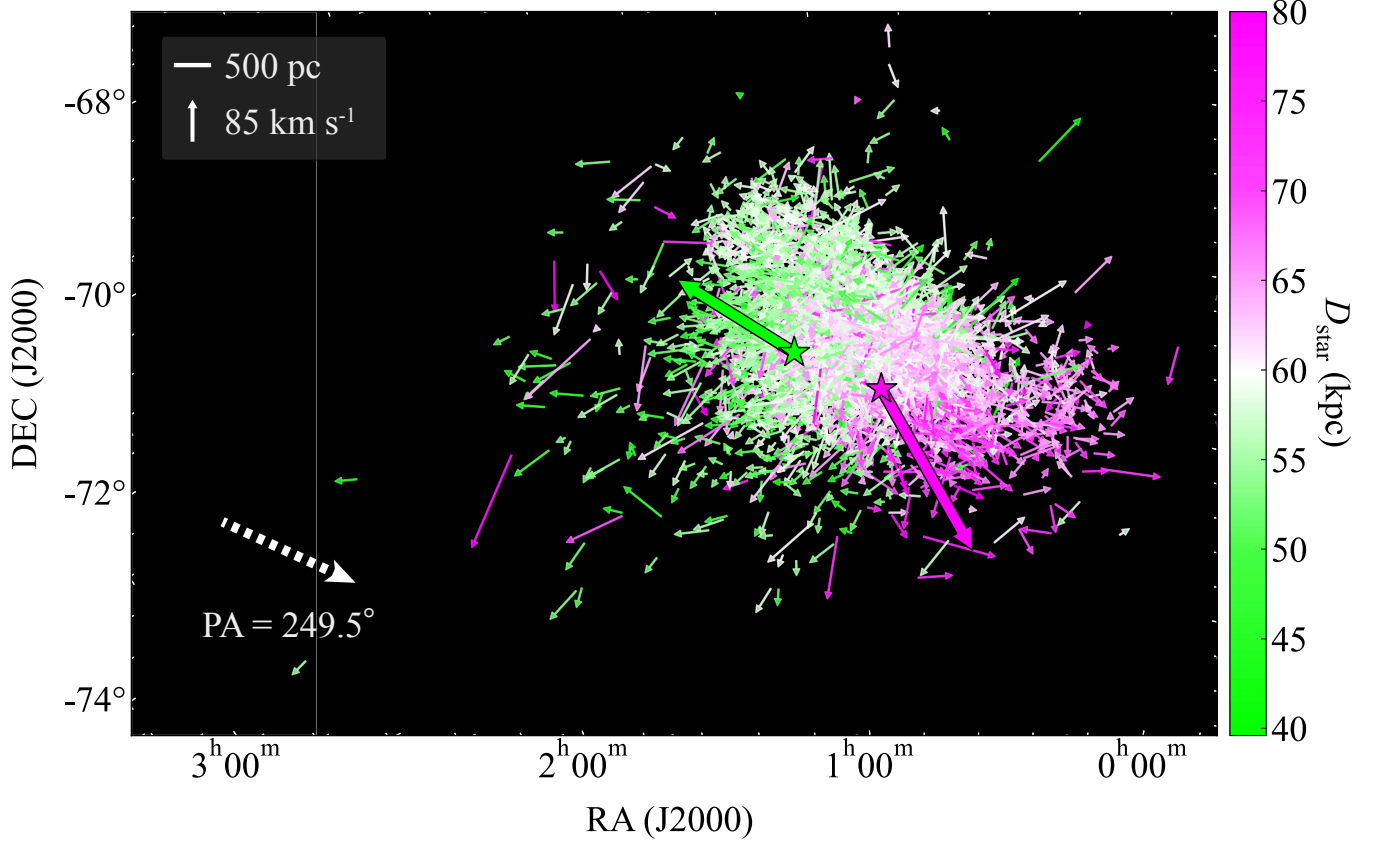
## 3. RESULTS

Figure 2 shows the internal PMs and  $D_{\text{star}}$  of the clipped CC samples obtained in Section 2. As demonstrated by V. Ripepi et al. (2017) and F. Niederhofer et al. (2021), the CCs exhibit a clear distance gradient extending from the northeast to the southwest (D. S. Mathewson et al. 1988). The position angle (PA) where the  $D_{\text{star}}$  gradient is most pronounced is  $249.5^{\circ}$ . Furthermore, our analysis reproduces the trend reported by F. Niederhofer et al. (2021), where nearer CCs move northeast relative to more distant ones. Since our analysis focuses on internal PMs, it is evident that nearer CCs move northeast, while more distant CCs move southwest, almost in opposite directions. In other words, in addition to the finding by F. Niederhofer et al. (2021) that nearer CCs are moving away from the main body, we find that more distant CCs are also receding from it. The outer CCs tend to move outward from the SMC, consistent with previous studies on various stellar populations based on internal PMs (e.g., P. Zivick et al. 2018; M. S. Oey et al. 2018; C. E. Murray et al. 2019; F. Niederhofer et al. 2021; S. Nakano et al. 2025). At the same time, the PMs of CCs do not exhibit a clear signature of galactic rotation. Only a few CCs are located in the southeastern Wing structure and the Magellanic Bridge. However, the small number of CCs distributed in the southeast move toward the LMC, suggesting an interaction with the LMC.

Figure 3 shows the internal PMs of the clipped CC samples, specifically highlighting those located at distant ( $>70$  kpc) and nearby ( $<55$  kpc) regions. The 241 distant CCs are predominantly found in the southwest, extending from the Bar, and generally move southwest. Those located in the northeast also exhibit motion toward the southwest. In contrast, a small number of distant CCs near the southeastern Wing move toward

<sup>4</sup> There are five other massive Cepheids without available  $D_{\text{star}}$  (see Figure 1), due to the saturation of the  $V$  magnitudes provided by OGLE-IV (A. Udalski et al. 2015; I. Soszyński et al. 2015).





**Figure 2.** The internal PMs of the clipped CC samples determined by subtracting the mean PM of the clipped CC samples. The legends indicate the magnitudes of PM vectors corresponding to  $85 \text{ km s}^{-1}$ , representing the minimum escape velocity derived under the assumption of H I rotation (S. Stanimirović et al. 2004; N. M. McClure-Griffiths et al. 2018). The colors of the PM vectors represent the distances  $D_{\text{star}}$  of the CCs, with more distant objects shown in magenta and nearer ones in green. The magenta and green star symbols indicate the mean positions of 241 distant ( $>70 \text{ kpc}$ ) and 276 nearby ( $<55 \text{ kpc}$ ) Cepheids, respectively. The thick vectors extending from the star symbols represent the mean PM vectors of the distant and nearby Cepheids, drawn at ten times the length of the individual stellar vectors for better visibility. Note that the distance thresholds for distant and nearby Cepheids (70 kpc and 55 kpc) are consistent with those used in F. Niederhofer et al. (2021). The white dotted arrow in the lower left of the figure indicates the direction in which the  $D_{\text{star}}$  gradient of the clipped CC samples is the largest.

the southeast. The westernmost distant CCs display somewhat random motions with relatively small magnitudes. The 276 nearby CCs are widely distributed east of the SMC and tend to move eastward, with their northward velocity increasing toward higher declinations. In the northeastern region, nearby CCs exhibit the prominent northeastward motion previously discovered by F. Niederhofer et al. (2021). Both distant and nearby CCs include a distinct population located in the northwest that moves northwest. When combined with the group moving southeast in the Wing, these findings indicate that the opposite motions in the eastern and western parts of the SMC, previously identified in massive star candidates by S. Nakano et al. (2025), are also present in CCs. This supports the interpretation, suggested by previous studies using internal PMs (e.g., P. Zivick et al. 2018; M. S. Oey et al. 2018; C. E. Murray et al. 2019;

F. Niederhofer et al. 2021; S. Nakano et al. 2025), that the SMC is being destructively elongated by the tidal forces and/or ram pressure exerted by the LMC, located to the southeast. The internal PM calculations accounting for the  $D_{\text{star}}$  of CCs demonstrate that the northwest-southeast elongation discovered by S. Nakano et al. (2025) is not merely a projection effect of distance. For further discussion on this elongation, including a comparison of the motions of massive star candidates and CCs, see also Appendix B.

Figure 4 shows the spatial distribution of the 91 clipped CC samples with available RVs, along with their RV values. The distribution of stars with available RVs closely resembles that of the massive star candidates (S. Nakano et al. 2025), clearly outlining the Bar structure extending from the southwest to the north of the SMC and the Wing structure stretching from the north to

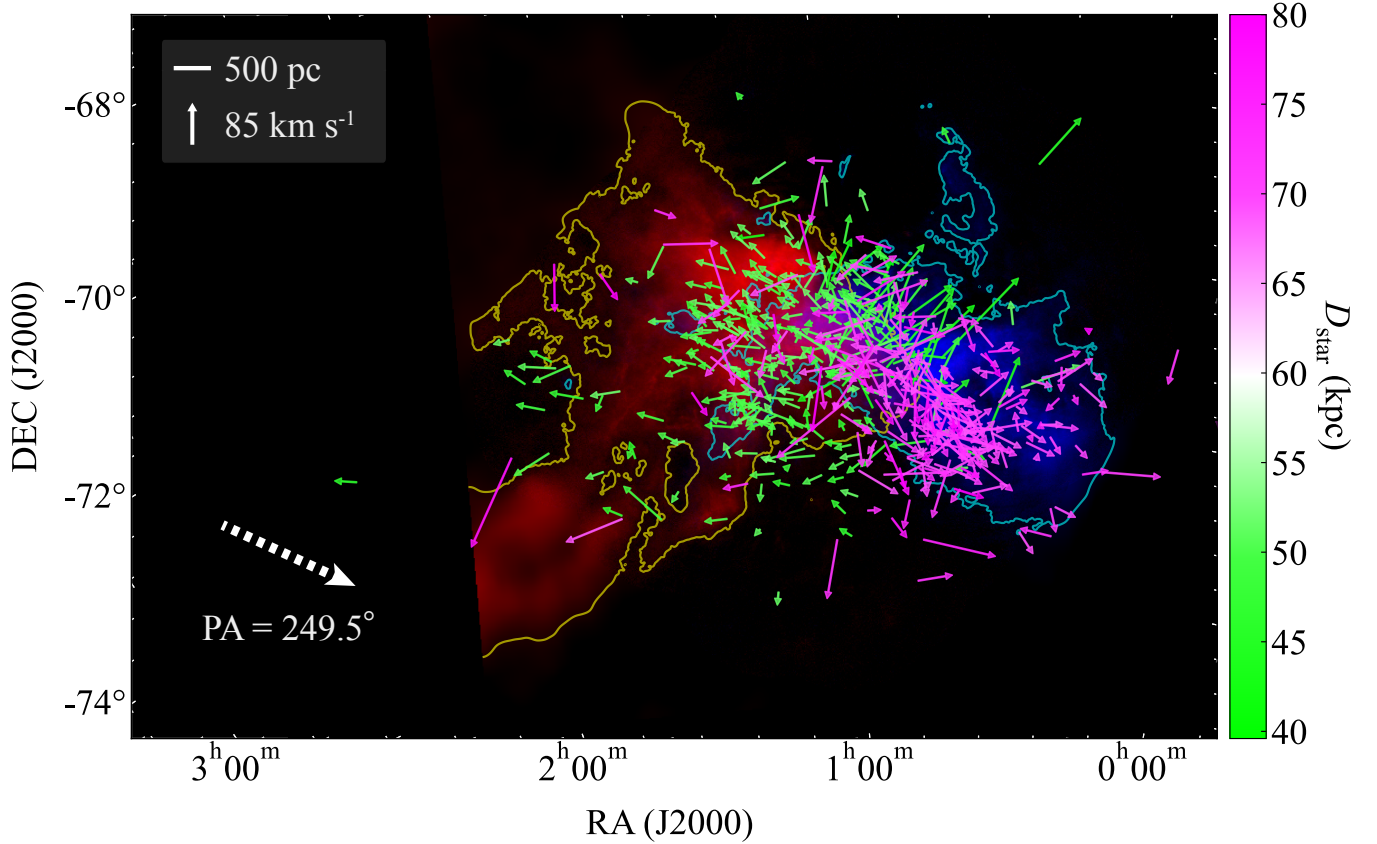


**Figure 3.** A comparison of the internal PMs of the clipped CC samples, considering only the 241 distant ( $>70$  kpc) and 276 nearby ( $<55$  kpc) populations, with the H I redshifted and blueshifted components. The magenta PM vectors represent the distant Cepheids ( $>70$  kpc), while the green PM vectors represent the nearby Cepheids ( $<55$  kpc). The background is a color multivelocity montage of the H I emission observed with ASKAP & Parkes (N. M. McClure-Griffiths et al. 2018), where red represents the integrated intensity for the 179–187  $\text{km s}^{-1}$  range, and blue for the 105–113  $\text{km s}^{-1}$  range, both displayed on a common logarithmic scale of 10–1000  $\text{K km s}^{-1}$ . Contours highlight the regions where the H I redshifted and blueshifted components are present, with yellow contours corresponding to the redshifted component and cyan contours to the blueshifted component. Note that these velocity components are consistent with those shown in Figure 2 of N. M. McClure-Griffiths et al. (2018). The white dotted arrow in the lower left of the figure indicates the direction in which the  $D_{\text{star}}$  gradient of the clipped CC samples is the largest.

the southeast. This is explained by the fact that CCs with available RVs in *Gaia* DR3 are bright stars with  $G \lesssim 15$  mag, meaning that relatively young stars, which can serve as ISM tracers, have been selected. The RVs of CCs decrease toward the northwest and increase toward the southeast. The  $PA$  at which the RV gradient is most pronounced is  $121.8^\circ$ . This trend is consistent with the RV distributions of various stellar populations, including red giants and massive stars (C. J. Evans & I. D. Howarth 2008; P. D. Dobbie et al. 2014; S. Nakano et al. 2025).

## 4. DISCUSSIONS

### 4.1. Comparison of CC Distances and Neutral Hydrogen Gas Velocity Components

Figure 3 compares the two velocity components of H I (a blueshifted component at approximately  $100 \text{ km s}^{-1}$ , and a redshifted component at approximately  $200 \text{ km s}^{-1}$ ) with the internal PMs of the clipped CC samples, specifically focusing on the distant ( $>70$  kpc) and nearby ( $<55$  kpc) populations. Distant CCs exhibit a spatial distribution similar to that of the H I blueshifted component, while nearby CCs resemble the H I redshifted component. Furthermore, the velocity gradient of H I at  $PA \sim 60^\circ$  (S. Stanimirović et al. 2004; E. M. Di Teodoro et al. 2019) is nearly parallel to the  $D_{\text{star}}$  gradient of CCs at  $PA = 249.5^\circ$ . The agreement in spatial distribution and gradient suggests

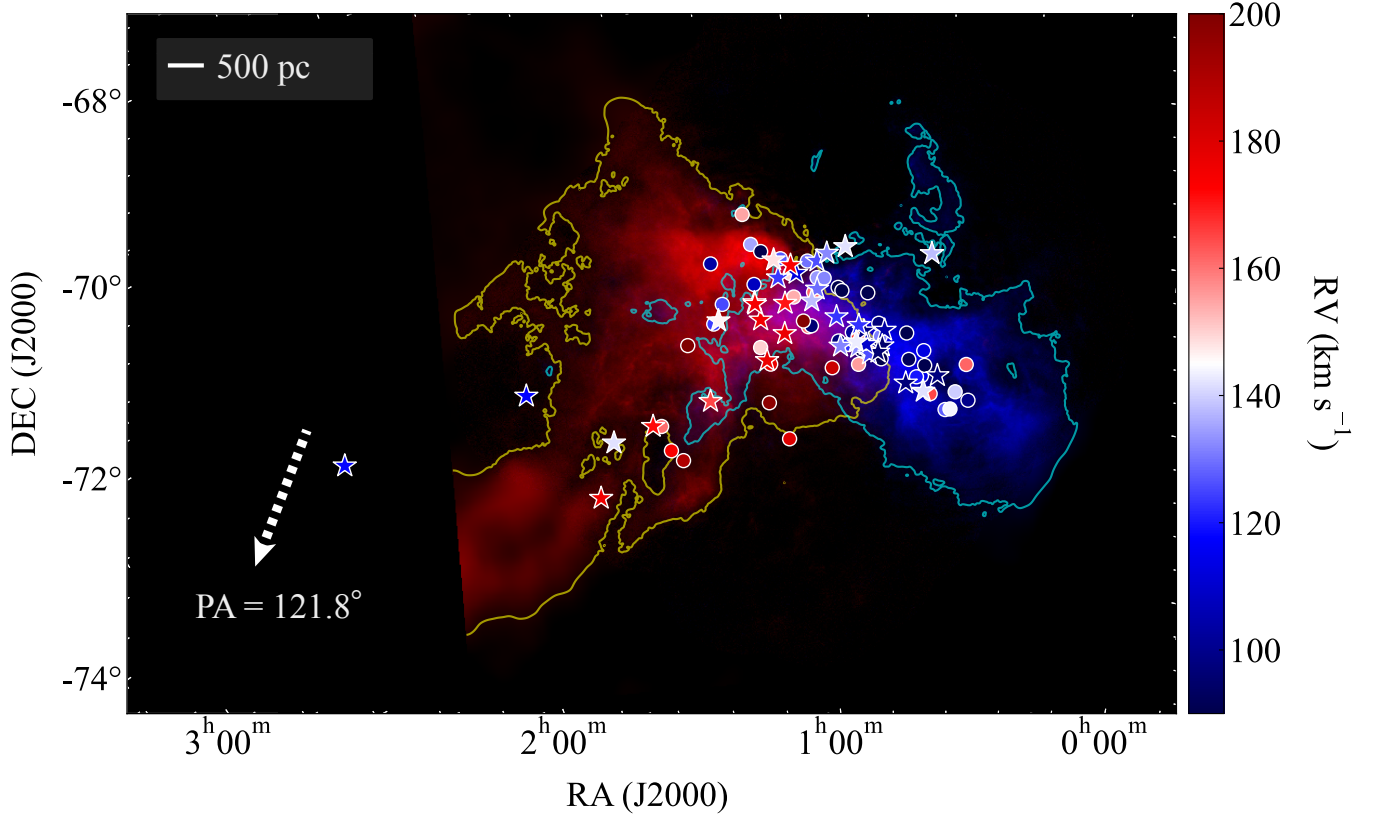


**Figure 4.** A comparison of the RVs of the 91 clipped CC samples with available RV data and the spatial distribution of the H I redshifted and blueshifted components. The star symbols represent 37 massive Cepheids that match the massive star candidates identified by [S. Nakano et al. \(2025\)](#) (see Figure 1). The circles indicate the remaining 54 CCs. The colors of the star symbols and circles correspond to the RV values of the CCs. In this figure, the RVs are shown in reference to the LSRK, consistent with the line-of-sight velocities of the H I. The white dotted arrow in the lower left of the figure indicates the direction in which the RV gradient is the largest.

that these components are physically related structures; that is, the H I blueshifted component may be located farther away and moving southwest, while the H I redshifted component may be positioned nearer and moving northeast. If this scenario is correct, the velocities of H I and the RVs of CCs should be consistent, meaning that nearer CCs should have larger RVs, while more distant CCs should have smaller RVs. In the next section, we discuss the relationship between the  $D_{\text{star}}$  and RVs of CCs.

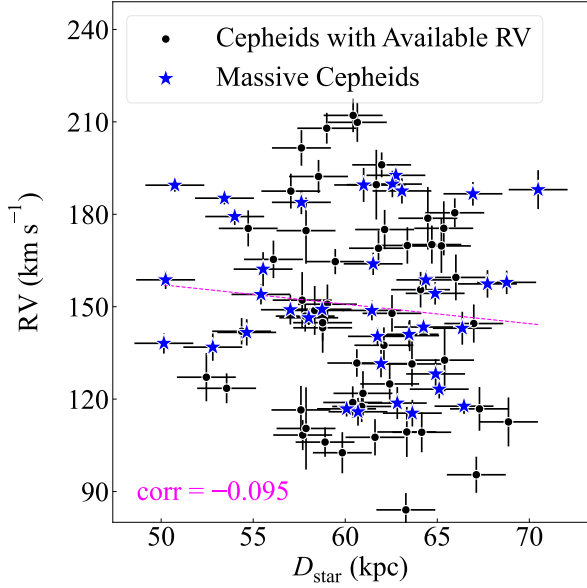
#### 4.2. No Correlation Between CCs' Distances and RVs

Figure 5 shows a plot of RV as a function of  $D_{\text{star}}$  for the 91 objects in the clipped CC sample with available RV measurements. The correlation coefficient between  $D_{\text{star}}$  and RV is  $-0.095$ , indicating they are nearly uncorrelated. This result remains unchanged even when considering only the 37 massive Cepheids, which serve

as gas tracers<sup>5</sup>. Thus, while the blueshifted/redshifted velocity components of H I and distant/nearby CCs appear to spatially coincide, they are kinematically inconsistent. The lack of correlation between  $D_{\text{star}}$  and RV suggests that the two observed gradients arise from distinct physical processes.

The difference in  $PA$  between the gradients of  $D_{\text{star}}$  and RVs supports the assertion that they originate from distinct mechanisms. The  $D_{\text{star}}$  gradient of CCs is oriented in the northeast-southwest direction, with  $PA = 249.5^\circ$ . In contrast, the RV gradient of CCs is oriented in the northwest-southeast direction, with  $PA = 121.8^\circ$ , indicating a clear discrepancy in their directions. Since this RV gradient direction is consistent with previous studies ([C. J. Evans & I. D. Howarth 2008](#); [P. D. Dobbie et al. 2014](#)), it cannot be explained as an apparent

<sup>5</sup> The correlation coefficient is  $-0.095$  when calculated for only massive Cepheids, and  $-0.097$  when calculated for the remaining CCs.



**Figure 5.** The relationship between  $D_{\text{star}}$  and RV for the 91 objects in the clipped CC samples with available RV measurements. The blue star symbols represent the 37 massive Cepheids that match the massive star candidates identified by S. Nakano et al. (2025) (see Figure 1), while the black circles indicate the remaining 54 CCs. The magenta dashed line represents the result of a linear fit, with a correlation coefficient of  $-0.095$  for the plotted data. The uncertainties in  $D_{\text{star}}$  are uniformly assumed to be 1.6 kpc (V. Ripepi et al. 2017).

gradient caused by the Wing structure detached from the main body of the SMC.

J. D. Diaz & K. Bekki (2012) demonstrated that tidal forces from the LMC induce a northwest-southeast line-of-sight velocity gradient in the spheroidal component of the SMC, suggesting that the northwest-southeast gradient observed in the RVs of CCs can be interpreted as an effect of the interaction with the LMC. Consequently, the northeast-southwest gradient seen in  $D_{\text{star}}$  of CCs may be a remnant of an earlier close encounter with the LMC. Alternatively, considering the  $\sim 20$ – $30$  kpc line-of-sight depth of the SMC, which is aligned with the Milky Way, it may be influenced by interaction between the Milky Way and the SMC.

Various studies measuring the RVs of different stellar populations (e.g., C. J. Evans & I. D. Howarth 2008; P. D. Dobbie et al. 2014; S. Nakano et al. 2025) have pointed out that the velocity gradient of stars ( $\sim 120^\circ$ ) does not align with that of H I ( $\sim 60^\circ$ ), contradicting expectations from galactic rotation. This discrepancy between the RV and H I velocity gradients closely resembles the inconsistency between the RV and  $D_{\text{star}}$  gradi-

ents of CCs. One possible explanation for this similarity is that while  $D_{\text{star}}$  of CCs traces the depth structure of H I, physical processes affecting only the gas—such as ram pressure or feedback from massive stars—have disrupted the velocity field of H I, leading to the observed mismatch between the RVs of stars and the velocity field of H I. However, the fact that even the RVs of 37 massive Cepheids with  $\text{Age} \lesssim 50.0$  Myr, as well as a larger number of massive star candidates identified by S. Nakano et al. (2025), do not align with the H I velocity field poses a significant challenge to this explanation. As previous studies on the internal PMs of stars in the SMC have suggested the SMC may lack galactic rotation (e.g., C. E. Murray et al. 2019; F. Niederhofer et al. 2021; S. Nakano et al. 2025), this challenge could potentially be addressed through numerical simulations assuming a non-rotating SMC.

Furthermore, Figure 5 does not show an increase in RVs proportional to  $D_{\text{star}}$ , which J. D. Diaz & K. Bekki (2012) cited as evidence for the Counter-Bridge (compare Figure 9 of J. D. Diaz & K. Bekki (2012) with Figure 5). Since the same result is obtained when considering only massive Cepheids, which serve as gas tracers, our findings appear robust. This may be because the Counter-Bridge is a structure formed from a rotating disk. If the SMC lacks galactic rotation, structures like the Counter-Bridge may not form. Additionally, the Counter-Bridge is an arched structure extending toward the LMC, which further highlights its inconsistency with the linearly extended line-of-sight depth observed in CCs (V. Ripepi et al. 2017). The absence of evidence for the Counter-Bridge also underscores the need for new numerical simulations. However, since the RV increase proportional to  $D_{\text{star}}$  in the Counter-Bridge becomes dominant at  $\gtrsim 70$  kpc, the lack of RV data for distant Cepheids in our sample may limit our ability to constrain the existence of the Counter-Bridge. Moreover, in various stellar populations, stars with low-velocity ( $\lesssim 150$  km s $^{-1}$ ) RVs, extending to  $\text{RA} \approx 2\text{h}$ , exhibit an inverted V-shaped distribution, indicating that the RV distribution cannot be explained by a simple unidirectional velocity gradient. This suggests the presence of a population with kinematics distinct from the main body of the SMC, which may be contaminating Figure 5. For a more precise discussion, additional RV measurements from *Gaia* DR4 are awaited.

We note that the massive Cepheids in Figure 5 exhibit a broader  $D_{\text{star}}$  distribution compared to other CCs with available RVs, while their RV range appears narrower. It is undeniable that young massive stars with  $\text{Age} \lesssim 50.0$  Myr also have a line-of-sight depth of  $\sim 20$  kpc. The significant line-of-sight depth of the mas-



sive stars, which serve as gas tracers, suggests that H I likely possesses a similarly line-of-sight depth. To clarify the distances to the massive stars and the associated gas beyond the CCs, we are attempting to constrain the distances through isochrone fitting of star clusters containing a large number of massive stars, with the results to be reported in a forthcoming paper.

## 5. SUMMARY AND CONCLUSIONS

Using *Gaia* DR3, we presented the distribution of internal PMs for 4,246 CCs, supported by their accurate distances, along with the relationship between  $D_{\text{star}}$  and RVs. The high-precision data from *Gaia* DR3 increased the number of CCs with available RVs from 8 to 91 compared to *Gaia* DR2. As a result, the internal PMs of CCs reproduced the motion reported by F. Niederhofer et al. (2021), where nearby CCs in the northeast move northeast relative to the distant CCs in the southwest. Furthermore, our internal PMs revealed that even the distant CCs move southwest relative to the main body. The distance gradient of the CCs is parallel to the line-of-sight velocity gradient of H I, but the RV gradient of the CCs is oriented differently from that of H I. The lack of correlation between the RVs and  $D_{\text{star}}$  of the CCs suggests that the two directional expansions indicated by their gradients were driven by different physical processes. Additionally, the CCs do not show the distance-dependent increase in RVs, which is observational evidence for the Counter-Bridge. Numerical simulations capable of reproducing these newly identified observational features are eagerly awaited.

## ACKNOWLEDGMENTS

This work was financially supported by JST SPRING, Grant Number JPMJSP2125. The author SN would like to take this opportunity to thank the “THERS Make New Standards Program for the Next Generation Researchers.” KT is supported in part by JSPS KAKENHI Grant Number 20H01945. SN would like to acknowledge the language assistance provided by ChatGPT (<https://chatgpt.com/>) and DeepL (<https://www.deepl.com/>) during the preparation of this manuscript. ChatGPT was particularly helpful in refining English expressions and enhancing the clarity of the text, while DeepL contributed to accurate and fluent translations. SN also wishes to express gratitude to OpenAI and DeepL SE for their technological contributions. This work has made use of data from the European Space Agency (ESA) mission *Gaia* (<https://www.cosmos.esa.int/gaia>), processed by the *Gaia* Data Processing and Analysis Consortium (DPAC, <https://www.cosmos.esa.int/web/>

[gaia/dpac/consortium](https://www.cosmos.esa.int/web/gaia/dpac/consortium)). Funding for the DPAC has been provided by national institutions, in particular the institutions participating in the *Gaia* Multilateral Agreement. This research has made use of the VizieR catalogue access tool, CDS, Strasbourg, France (F. Ochsenbein 1996). The original description of the VizieR service was published in F. Ochsenbein et al. (2000). This scientific work uses data obtained from Inyarrimanha Ilgari Bundara, the CSIRO Murchison Radio-astronomy Observatory. We acknowledge the Wajarri Yamaji People as the Traditional Owners and native title holders of the Observatory site. CSIRO’s ASKAP radio telescope and Murriyang, CSIRO’s Parkes radio telescope, are part of the Australia Telescope National Facility (<https://ror.org/05qajvd42>). Operation of ASKAP is funded by the Australian Government with support from the National Collaborative Research Infrastructure Strategy. Parkes is funded by the Australian Government for operation as a National Facility managed by CSIRO. ASKAP uses the resources of the Pawsey Supercomputing Research Centre. Establishment of ASKAP, Inyarrimanha Ilgari Bundara, the CSIRO Murchison Radio-astronomy Observatory and the Pawsey Supercomputing Research Centre are initiatives of the Australian Government, with support from the Government of Western Australia and the Science and Industry Endowment Fund.

*Facilities:* *Gaia*, ASKAP, Parkes

*Software:* *aplpy* (T. Robitaille & E. Bressert 2012), *astropy* (Astropy Collaboration et al. 2013, 2018), *CASA* (J. P. McMullin et al. 2007), *ChatGPT* (OpenAI et al. 2024), *dustapprox* (M. Fouesneau et al. 2022), *matplotlib* (J. D. Hunter 2007)

## APPENDIX

## A. CATALOG OF 4,236 CLASSICAL CEPHEIDS IN THE SMC

**Table 1.** Cross-match Results between *Gaia* DR3 and OGLE-IV

	<i>Gaia</i> DR3 ID	OGLE ID	RA (J2000)	DEC (J2000)	<i>G</i>	$\sigma_G$	...	$D_{\text{star}}$	...
			(deg)	(deg)	(mag)	(mag)		(kpc)	
0	4688994540756312448	OGLE-SMC-CEP-2476	13.99184887489	-72.44262025649	19.706955	0.006493	...	76.7	...
1	4689077656954612224	OGLE-SMC-CEP-2095	13.42241613345	-72.01297635880	18.745564	0.011079	...	55.2	...
2	4688685577930565760	OGLE-SMC-CEP-0022	5.89227970642	-73.39970785978	19.047304	0.006729	...	66.9	...
3	4687626365985065088	OGLE-SMC-CEP-4548	19.41465531930	-71.63650902714	18.945671	0.007297	...	73.0	...

Here we only show part of the table. The machine readable table will be available in the HTML version of the article.

NOTE—The complete table includes the following: the SOURCE\_ID of *Gaia* DR3 (**Gaia-DR3-ID**) and OGLE (**OGLE-ID**), coordinates in J2000 (**RAdeg**, **DEdeg**), photometry for *G*, *G*<sub>BP</sub>, and *G*<sub>RP</sub> (**Gmag**, **GBPmag**, and **GRPmag**), the parallax and its uncertainty (**plx**), the *Gaia* PMs (**pmRA**, **pmDE**), the distances  $D_{\text{star}}$  calculated assuming  $D_{\text{SMC}} = 62$  kpc (**Dstar**; see Section 2.1), the *Gaia* radial velocities and their uncertainties (**RVel**), flags of the PM 2 $\sigma$ -cutoff samples (**PM-2s-clip**; see Section 2.3), the internal PMs within the SMC calculated in Section 2.3 (**pmRA-in**, **pmDE-in**), the internal PMs respect to massive star candidates of S. Nakano et al. (2025) calculated in Appendix B (**pmRA-in-OB**, **pmDE-in-OB**).

## B. INTERNAL PMS OF CCS WITH RESPECT TO YOUNG MASSIVE STARS

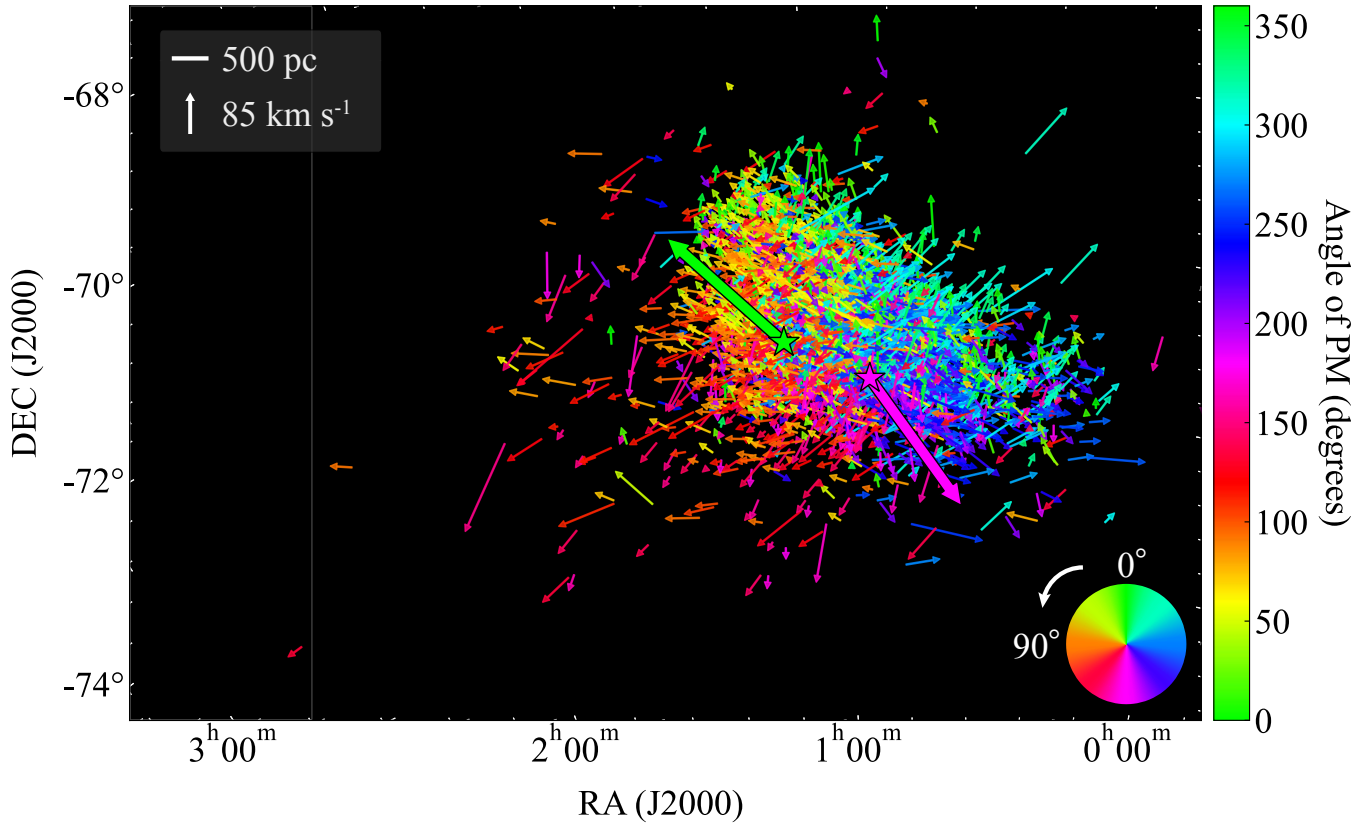
In this section, we compare the internal PMs of the massive star candidates from S. Nakano et al. (2025) with those of the CCs. In the calculations in Section 2.3, we instead use the mean PM of the massive star candidates  $(\mu_\alpha, \mu_\delta) = (0.785, -1.245)$  mas yr<sup>-1</sup> (S. Nakano et al. 2025) for the systemic PM of the SMC, and the dynamical center of the H I gas  $(\alpha_{\text{H I}}, \delta_{\text{H I}}) = (16.26^\circ, -72.42^\circ)$  (S. Stanimirović et al. 2004) as the coordinate center. A major difference is that the mean PM of the massive star candidates accounts for the motion of stars distributed in the Wing. The newly computed internal PMs of CCs referenced to the massive star candidates are listed in Section A.

Figure 6 shows the internal PMs of the clipped CC samples obtained relative to the mean PM of the massive star candidates. The mean PMs of the distant and nearby CCs shown in Figure 6 are more parallel compared to those shown in Figure 2, making it clearer that they move in opposite directions along the distance gradient. This suggests that the near-far extension observed in the CCs (F. Niederhofer et al. 2021) occurs relative to the dynamical center of the H I gas, rather

than the distribution center of the CCs (V. Ripepi et al. 2017).

Figure 6 is similar to the distribution of the internal PMs of massive star candidates shown in Figure 10 of S. Nakano et al. (2025), with stars in the southeast moving southeast and stars in the northwest moving northwest. On the other hand, the northeast-southwest extension shown by F. Niederhofer et al. (2021) is not observed in the massive star candidates and is a feature found only in the CCs.

Figure 7 shows the median PMs of the CCs, which overlap with the positions of the Superstructures identified by S. Nakano et al. (2025), which correspond to the  $\sim 100$  pc scale concentrations of massive stars classified by their surface density. This provides an overview of the average internal PMs of the more central regions of the SMC. Similar to the motion of the Superstructures shown in Figure 14 of S. Nakano et al. (2025), in Superstructure 3, a motion towards the LMC is observed, while in Superstructures 7 and 9, motions away from the LMC are seen. The northwest-directed motion of Superstructure 7 highlights the dominant northwestward movement of the CCs in the northwest, regardless of distance, as shown in Figure 3. The lack of clear motion in Superstructure 8 and the westward motion in Superstructure 9 can be attributed to the dominant south-



**Figure 6.** The internal PMs of the clipped CC samples, obtained by subtracting the mean PM of the massive star candidates (S. Nakano et al. 2025). The color of the PM vectors represents their direction, with the angle defined counterclockwise from north ( $0^\circ$ ) in the  $(x, y)$  coordinates based on the the orthographic projection centered on the H I dynamical center (S. Stanimirović et al. 2004). The magenta and green star symbols represent the mean positions of the distant ( $>70$  kpc) and nearby ( $<55$  kpc) Cepheids, respectively. The thick vectors extending from the star symbols indicate the mean PM vectors of the distant and nearby Cepheids, drawn at ten times the length of individual stellar vectors for better visibility.

westward motion observed in the distant CCs, which are more concentrated in the southwest.

The CCs are located at approximately the same distance at the positions of Superstructure 5 and 6 (with medians of 58.0 kpc and 60.0 kpc, respectively), with both groups moving towards the northeast. This contrasts with that reported by S. Nakano et al. (2025), where different directions of motion were observed for Superstructure 4, 5, and 6 under the assumption that all the massive star candidates are at the same distance. This suggests that either young massive star candidates in Superstructures 5 and 6 are at different distances, or they are at the same distance but exhibit different motions. In either case, at the positions of Superstructures 5 and 6, the CCs and the massive star candidates exhibit different properties. This fact supports assertion of S. Nakano et al. (2025) that the distribution and mo-

tion of massive star candidates differ from those of the older population.

Note that there are more massive star candidates with larger PMs that would escape from the SMC. This suggests the possibility that recent star formation is occurring in gas that has escaped the SMC due to the tidal interaction, ram pressure or feedback. Furthermore, while the CCs are distributed in the southern region of the SMC, neither the massive star candidates nor the ISM are found in the southern region of the SMC. This separation may imply that not only tidal forces from the LMC but also ram pressure and/or feedback have acted towards the LMC direction. In Figure 6, the internal PMs of the CCs located in the southern SMC are polarized into two directions—southwest and southeast—indicating that stars being stripped from the bar are moving southeast.

## REFERENCES

- Astropy Collaboration, Robitaille, T. P., Tollerud, E. J., et al. 2013, *A&A*, 558, A33, doi: [10.1051/0004-6361/201322068](https://doi.org/10.1051/0004-6361/201322068)
- Astropy Collaboration, Price-Whelan, A. M., Sipőcz, B. M., et al. 2018, *AJ*, 156, 123, doi: [10.3847/1538-3881/aabc4f](https://doi.org/10.3847/1538-3881/aabc4f)

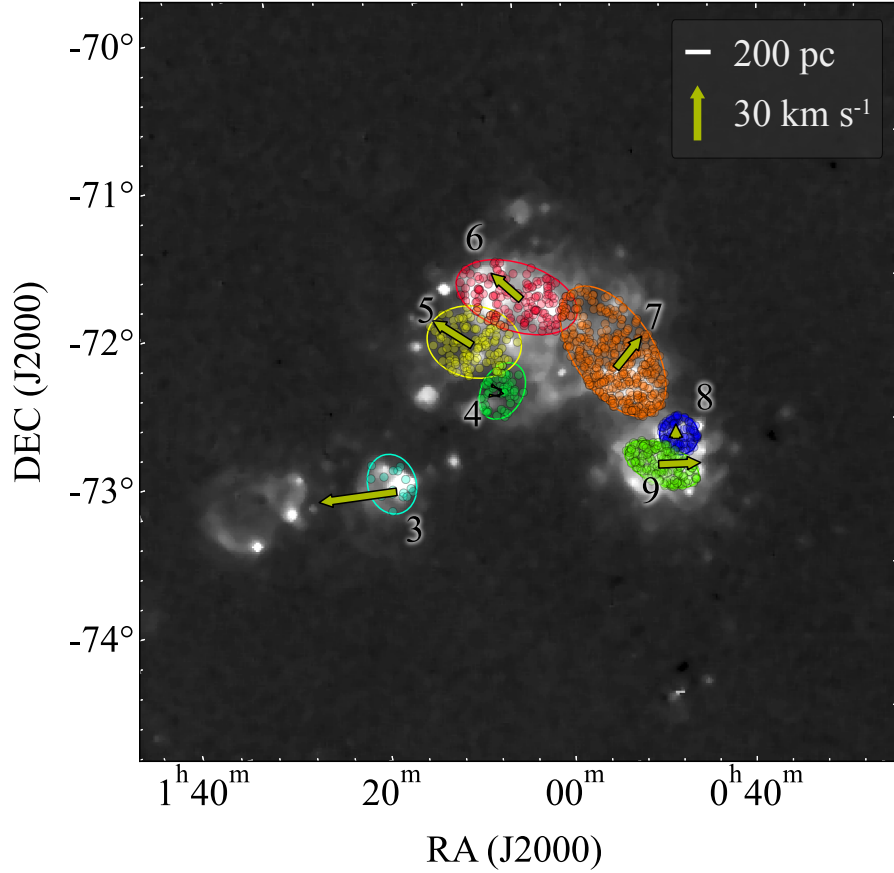


**Figure 7.** The median PMs of the clipped CC samples at locations corresponding to each Superstructure (S. Nakano et al. 2025). The median PMs are derived from the clipped CC samples located within the  $2\sigma$  elliptical regions, defined using the half-number radius of each Superstructure, as listed in Table 2 of S. Nakano et al. (2025). Since the ellipses of Superstructure 1 and 2 contain only 0 and 3 CCs, respectively, their median values are not statistically significant and are therefore omitted from this figure. The background displays H $\alpha$  emission from SHASSA in the range of 0–600 deciRayleighs (dR; J. E. Gaustad et al. 2001).

- Besla, G., Kallivayalil, N., Hernquist, L., et al. 2007, *ApJ*, 668, 949, doi: [10.1086/521385](https://doi.org/10.1086/521385)
- Besla, G., Kallivayalil, N., Hernquist, L., et al. 2012, *MNRAS*, 421, 2109, doi: [10.1111/j.1365-2966.2012.20466.x](https://doi.org/10.1111/j.1365-2966.2012.20466.x)
- Bressan, A., Marigo, P., Girardi, L., et al. 2012, *MNRAS*, 427, 127, doi: [10.1111/j.1365-2966.2012.21948.x](https://doi.org/10.1111/j.1365-2966.2012.21948.x)
- Chen, Y., Bressan, A., Girardi, L., et al. 2015, *MNRAS*, 452, 1068, doi: [10.1093/mnras/stv1281](https://doi.org/10.1093/mnras/stv1281)
- Chen, Y., Girardi, L., Bressan, A., et al. 2014, *MNRAS*, 444, 2525, doi: [10.1093/mnras/stu1605](https://doi.org/10.1093/mnras/stu1605)
- Cioni, M. R. L., Clementini, G., Girardi, L., et al. 2011, *A&A*, 527, A116, doi: [10.1051/0004-6361/201016137](https://doi.org/10.1051/0004-6361/201016137)
- de Grijs, R., & Bono, G. 2015, *AJ*, 149, 179, doi: [10.1088/0004-6256/149/6/179](https://doi.org/10.1088/0004-6256/149/6/179)
- de Grijs, R., Wicker, J. E., & Bono, G. 2014, *AJ*, 147, 122, doi: [10.1088/0004-6256/147/5/122](https://doi.org/10.1088/0004-6256/147/5/122)
- De Leo, M., Carrera, R., Noël, N. E. D., et al. 2020, *MNRAS*, 495, 98, doi: [10.1093/mnras/staa1122](https://doi.org/10.1093/mnras/staa1122)
- Di Teodoro, E. M., McClure-Griffiths, N. M., Jameson, K. E., et al. 2019, *MNRAS*, 483, 392, doi: [10.1093/mnras/sty3095](https://doi.org/10.1093/mnras/sty3095)
- Diaz, J. D., & Bekki, K. 2012, *ApJ*, 750, 36, doi: [10.1088/0004-637X/750/1/36](https://doi.org/10.1088/0004-637X/750/1/36)
- Dobbie, P. D., Cole, A. A., Subramaniam, A., & Keller, S. 2014, *MNRAS*, 442, 1663, doi: [10.1093/mnras/stu910](https://doi.org/10.1093/mnras/stu910)
- Evans, C. J., & Howarth, I. D. 2008, *MNRAS*, 386, 826, doi: [10.1111/j.1365-2966.2008.13012.x](https://doi.org/10.1111/j.1365-2966.2008.13012.x)
- Fouesneau, M., Andrae, R., Sordo, R., & Dharmawardena, T. 2022, 0.1 <https://github.com/mfouesneau/dustapprox>
- Gaia Collaboration, Prusti, T., de Bruijne, J. H. J., et al. 2016, *A&A*, 595, A1, doi: [10.1051/0004-6361/201629272](https://doi.org/10.1051/0004-6361/201629272)
- Gaia Collaboration, Helmi, A., van Leeuwen, F., et al. 2018, *A&A*, 616, A12, doi: [10.1051/0004-6361/201832698](https://doi.org/10.1051/0004-6361/201832698)



- Gaia Collaboration, Vallenari, A., Brown, A. G. A., et al. 2023, *A&A*, 674, A1, doi: [10.1051/0004-6361/202243940](https://doi.org/10.1051/0004-6361/202243940)
- Gaustad, J. E., McCullough, P. R., Rosing, W., & Van Buren, D. 2001, *PASP*, 113, 1326, doi: [10.1086/323969](https://doi.org/10.1086/323969)
- Graczyk, D., Pietrzyński, G., Thompson, I. B., et al. 2014, *ApJ*, 780, 59, doi: [10.1088/0004-637X/780/1/59](https://doi.org/10.1088/0004-637X/780/1/59)
- Hindman, J. V., Kerr, F. J., & McGee, R. X. 1963, *Australian Journal of Physics*, 16, 570, doi: [10.1071/PH630570](https://doi.org/10.1071/PH630570)
- Hunter, J. D. 2007, *Computing in Science and Engineering*, 9, 90, doi: [10.1109/MCSE.2007.55](https://doi.org/10.1109/MCSE.2007.55)
- Irwin, M. J., Kunkel, W. E., & Demers, S. 1985, *Nature*, 318, 160, doi: [10.1038/318160a0](https://doi.org/10.1038/318160a0)
- Jacyszyn-Dobrzeńicka, A. M., Skowron, D. M., Mróz, P., et al. 2017, *AcA*, 67, 1, doi: [10.32023/0001-5237/67.1.1](https://doi.org/10.32023/0001-5237/67.1.1)
- Marigo, P., Girardi, L., Bressan, A., et al. 2017, *ApJ*, 835, 77, doi: [10.3847/1538-4357/835/1/77](https://doi.org/10.3847/1538-4357/835/1/77)
- Mathewson, D. S., Cleary, M. N., & Murray, J. D. 1974, *ApJ*, 190, 291, doi: [10.1086/152875](https://doi.org/10.1086/152875)
- Mathewson, D. S., Ford, V. L., & Visvanathan, N. 1988, *ApJ*, 333, 617, doi: [10.1086/166772](https://doi.org/10.1086/166772)
- McClure-Griffiths, N. M., Dénes, H., Dickey, J. M., et al. 2018, *Nature Astronomy*, 2, 901, doi: [10.1038/s41550-018-0608-8](https://doi.org/10.1038/s41550-018-0608-8)
- McMullin, J. P., Waters, B., Schiebel, D., Young, W., & Golap, K. 2007, in *Astronomical Society of the Pacific Conference Series*, Vol. 376, *Astronomical Data Analysis Software and Systems XVI*, ed. R. A. Shaw, F. Hill, & D. J. Bell, 127
- Muller, E., & Bekki, K. 2007, *MNRAS*, 381, L11, doi: [10.1111/j.1745-3933.2007.00356.x](https://doi.org/10.1111/j.1745-3933.2007.00356.x)
- Murray, C. E., Peek, J. E. G., Di Teodoro, E. M., et al. 2019, *ApJ*, 887, 267, doi: [10.3847/1538-4357/ab510f](https://doi.org/10.3847/1538-4357/ab510f)
- Nakano, S., Tachihara, K., & Tamashiro, M. 2025, *arXiv e-prints*, arXiv:2502.12251, doi: [10.48550/arXiv.2502.12251](https://doi.org/10.48550/arXiv.2502.12251)
- Niederhofer, F., Cioni, M.-R. L., Rubele, S., et al. 2021, *MNRAS*, 502, 2859, doi: [10.1093/mnras/stab206](https://doi.org/10.1093/mnras/stab206)
- Ochsenbein, F. 1996, *CDS, Centre de Données astronomiques de Strasbourg*, doi: [10.26093/CDS/VIZIER](https://doi.org/10.26093/CDS/VIZIER)
- Ochsenbein, F., Bauer, P., & Marcout, J. 2000, *A&AS*, 143, 23, doi: [10.1051/aas:2000169](https://doi.org/10.1051/aas:2000169)
- Oey, M. S., Dorigo Jones, J., Castro, N., et al. 2018, *ApJL*, 867, L8, doi: [10.3847/2041-8213/aae892](https://doi.org/10.3847/2041-8213/aae892)
- OpenAI, :, Hurst, A., et al. 2024, *arXiv e-prints*, arXiv:2410.21276, doi: [10.48550/arXiv.2410.21276](https://doi.org/10.48550/arXiv.2410.21276)
- Pastorelli, G., Marigo, P., Girardi, L., et al. 2019, *MNRAS*, 485, 5666, doi: [10.1093/mnras/stz725](https://doi.org/10.1093/mnras/stz725)
- Pastorelli, G., Marigo, P., Girardi, L., et al. 2020, *MNRAS*, 498, 3283, doi: [10.1093/mnras/staa2565](https://doi.org/10.1093/mnras/staa2565)
- Ripepi, V., Marconi, M., Moretti, M. I., et al. 2016, *ApJS*, 224, 21, doi: [10.3847/0067-0049/224/2/21](https://doi.org/10.3847/0067-0049/224/2/21)
- Ripepi, V., Cioni, M.-R. L., Moretti, M. I., et al. 2017, *MNRAS*, 472, 808, doi: [10.1093/mnras/stx2096](https://doi.org/10.1093/mnras/stx2096)
- Robitaille, T., & Bressert, E. 2012, *Astrophysics Source Code Library*, record ascl:1208.017
- Salem, M., Besla, G., Bryan, G., et al. 2015, *ApJ*, 815, 77, doi: [10.1088/0004-637X/815/1/77](https://doi.org/10.1088/0004-637X/815/1/77)
- Soszyński, I., Udalski, A., Szymański, M. K., et al. 2015, *AcA*, 65, 297, doi: [10.48550/arXiv.1601.01318](https://doi.org/10.48550/arXiv.1601.01318)
- Stanimirović, S., Staveley-Smith, L., & Jones, P. A. 2004, *ApJ*, 604, 176, doi: [10.1086/381869](https://doi.org/10.1086/381869)
- Tang, J., Bressan, A., Rosenfield, P., et al. 2014, *MNRAS*, 445, 4287, doi: [10.1093/mnras/stu2029](https://doi.org/10.1093/mnras/stu2029)
- Udalski, A., Szymański, M. K., & Szymański, G. 2015, *AcA*, 65, 1, doi: [10.48550/arXiv.1504.05966](https://doi.org/10.48550/arXiv.1504.05966)
- Zivick, P., Kallivayalil, N., van der Marel, R. P., et al. 2018, *ApJ*, 864, 55, doi: [10.3847/1538-4357/aad4b0](https://doi.org/10.3847/1538-4357/aad4b0)